

Rheology of three dimensional granular chute flows at large inertial numbers

Satyabrata Patro and Anurag Tripathi*

Department of Chemical Engineering, Indian Institute of Technology Kanpur, Uttar Pradesh, 208016, India

(Dated: May 16, 2024)

The inertial number-based rheology, popularly known as the JFP model, is well known for describing the rheology of granular materials in the dense flow regime. While most of the recent studies focus on the steady-state rheology of granular materials, the time-dependent rheology of such materials has received less attention. Owing to this fact, we perform three-dimensional DEM simulations of frictional inelastic spheres flowing down an inclined bumpy surface varying over a wide range of inclination angles and restitution coefficients. We show that steady, fully developed flows are possible at inclinations much higher than those predicted from the JFP model rheology. We show that, in addition to a modified effective friction law, the rheological description also needs to account for the stress anisotropy by means of a first and second normal stress difference law.

I. INTRODUCTION

The rheology of granular materials has been an active research topic for the last few decades due to its wide occurrence in geophysical as well as industrial situations. A number of experimental [1–18] as well as simulation studies using discrete element method (DEM) [2, 19–34] have been utilized to explore the rheology of granular materials. A detailed review of granular flow rheology in different configurations can be found in [35–37]. These studies have shown that the granular flow between the two limiting cases of quasistatic, slow flows, and rapid, dilute flows is controlled by a non-dimensional inertial number $I = d\dot{\gamma}/\sqrt{P/\rho_p}$, which depends on the local shear rate $\dot{\gamma}$ and pressure P in addition to the particle size d and density ρ_p . In our previous study, we investigated the rheology of two-dimensional granular chute flows at high inertial numbers and showed that the popularly used JFP model with a saturating behavior of the effective friction coefficient at high inertial numbers fails to capture the rheology at high inertial numbers [32]. Instead, a non-monotonic variation of $\mu(I)$ is observed at large inertial numbers with a maximum at $I \approx 0.8$. The non-monotonic variation of the effective friction coefficient μ , along with a weak power law relation of the solids fraction ϕ and a normal stress difference law N_1/P with the inertial number I has also been proposed in Patro *et al.* [32] which describes the rheology at large inertial numbers. Now, we explore the rheology of three-dimensional granular chute flows for a wide range of inclination angles and check whether the flow behavior observed in the 2D DEM simulations is observable in 3D DEM simulations as well.

Hence, we investigate the rheology of slightly polydisperse, inelastic spheres flowing down a rough inclined plane using discrete element method (DEM) simulations over a wide range of inclination angles. Two different layer heights in the settled configuration of $L_y = 20d$ and $L_y = 40d$ are considered. We show that steady, fully developed flows are possible at high inertial numbers $I > 0.8$. We also show that in addition to the first normal stress difference which was found to be significant in 2D, the second normal stress difference also becomes important in the case of 3D flows. The restitution coefficient considered in this study is $e_n = 0.5$. Due to the classical results of Silbert *et al.* [19], which showed that the restitution coefficient has no significant role in the case of sufficiently frictional grains, most studies typically use normal coefficient of restitution close to $e_n = 0.9$. Our results shown in Patro *et al.* [32] show that using this default choice of restitution coefficient, the observation of transition from dense to dilute regime becomes very difficult since a small change in the inclination angle leads to accelerating flows. In order to obtain a large range of inclination angles at which non-accelerating flows are observable, we use these lower values of normal coefficient of restitution. We wish to emphasize the fact that the choice of restitution coefficient $e_n = 0.5$ is not unrealistic and quite a few studies [38–46] report the restitution coefficient of industrial grains near 0.5.

II. SIMULATION METHODOLOGY

In the previous study, we investigated the rheology of two-dimensional granular chute flows at high inertial numbers and showed that the popularly used JFP model with a saturating behavior of the effective friction coefficient at high inertial numbers fails to capture the rheology at high inertial numbers. Instead, a non-monotonic variation of $\mu(I)$ is

* anuragt@iitk.ac.in

observed at large inertial numbers with a maximum at $I \approx 0.8$. The non-monotonic variation of the effective friction coefficient μ , along with a weak power law relation of the solids fraction ϕ and a normal stress difference law N_1/P with the inertial number I has also been proposed in Patro *et al.* [32] which describes the rheology at large inertial numbers. Now, we explore the rheology of three-dimensional granular chute flows for a wide range of inclination angles and check whether the flow behavior observed in the 2D DEM simulations is observable in 3D DEM simulations as well.

Hence, we investigate the rheology of slightly polydisperse, inelastic spheres flowing down a rough inclined plane using discrete element method (DEM) simulations over a wide range of inclination angles. Two different layer heights in the settled configuration of $L_y = 20d$ and $L_y = 40d$ are considered. We show that steady, fully developed flows are possible at high inertial numbers $I > 0.8$. We also show that in addition to the first normal stress difference which was found to be significant in 2D, the second normal stress difference also becomes important in the case of 3D flows. The restitution coefficient considered in this study is $e_n = 0.5$. Due to the classical results of Silbert *et al.* [19], which showed that the restitution coefficient has no significant role in the case of sufficiently frictional grains, most studies typically use normal coefficient of restitution close to $e_n = 0.9$. Our results in Patro *et al.* [32] show that using this default choice of restitution coefficient, the observation of transition from dense to dilute regime becomes very difficult since a small change in the inclination angle leads to accelerating flows. In order to obtain a large range of inclination angles at which non-accelerating flows are observable, we use these lower values of normal coefficient of restitution. We wish to emphasize the fact that the choice of restitution coefficient 0.5 is not unrealistic and quite a few studies [38–46] report the restitution coefficient of industrial grains near 0.5.

III. SIMULATION METHODOLOGY

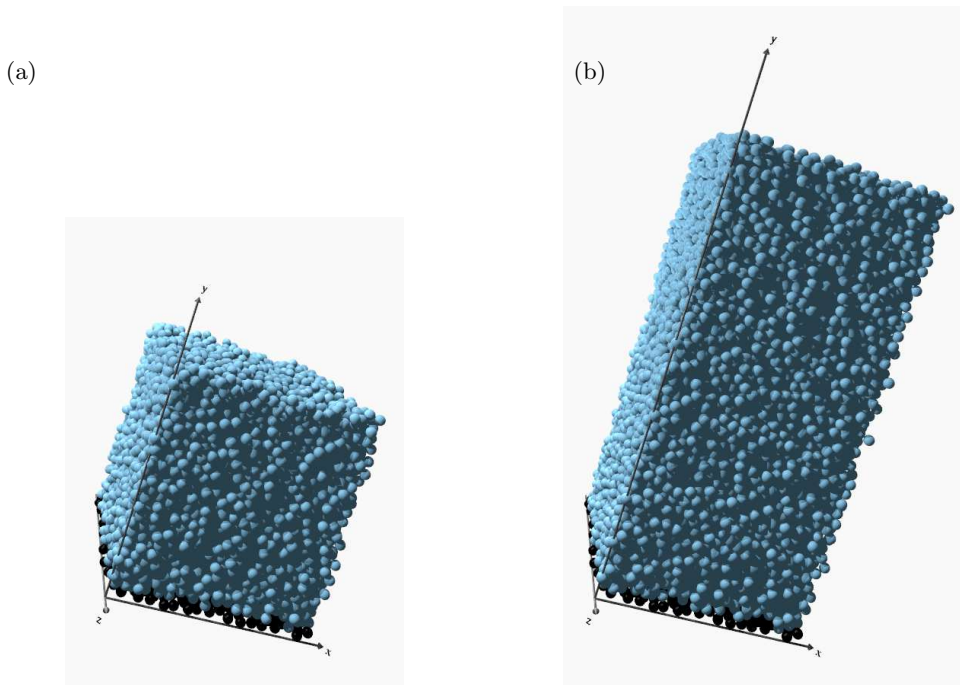


FIG. 1. Chute flow simulation setup of dimension a) $20d \times 20d \times 20d$, and b) $20d \times 40d \times 20d$. black spheres represent the moving particles whereas the black spheres represent the static particles used to create a bumpy base. Periodic boundary conditions are used in the flow (x) and vorticity (z) direction.

The discrete element method (DEM) is used to perform three-dimensional simulations of slightly polydisperse particles ($\pm 5\%$ polydispersity) of mean diameter $d = 1\text{mm}$ flowing down a rough and bumpy inclined surface. The bumpy base is made of static spheres of diameter $2d$. The schematic view of the simulation setup is shown in Fig. 1 where the blue spheres represent the flowing particles and black spheres represent the static particles of the bumpy base. The length and width of the simulation box is $L_x = L_z = 20d$ along the x and z direction. The height of the simulation box is kept sufficiently large so that the particles do not feel the presence of the upper surface. In order to simulate an infinitely long inclined flow without end effects and neglect the variation in the vorticity direction,

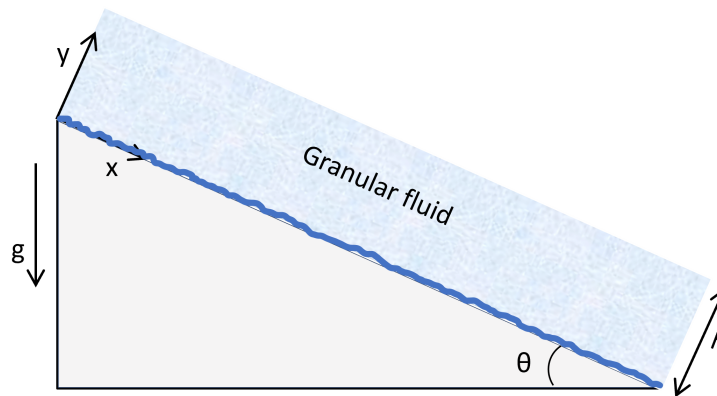


FIG. 2. Schematic of the chute flow geometry. The black-shaded region represents the granular fluid. The uneven surface near the base of the granular fluid represents the bumpy base.

periodic boundary conditions are used in the flow (x) and vorticity (z) direction. Fig. 1(a) shows the simulation setup where the settled layer height is $L_y = 20d$ and fig. 1(b) shows the simulation setup where the settled layer height is $L_y = 40d$. The number of particles in the first case is $N_p = 8000$ whereas the number of particles in the second case is $N_p = 16000$.

Particles are modeled as soft, deformable, inelastic, frictional spheres. The contact force between the spheres is modeled using the Hertz-Mindlin model in the LIGGGHTS-PUBLIC 3.0 open-source DEM package. The details about the contact force models, particle generation, particle settling, and property calculation are given in detail in Patro *et al.* [32].

Consider the steady and fully developed granular flow over a surface inclined at an angle θ under the influence of gravity. The schematic of granular fluid flowing down an inclined plane is shown in Figure 2. Assuming a unidirectional flow in the x -direction, the momentum balance equations in x and y direction simplify to

$$0 = -\frac{\partial \tau_{yx}}{\partial y} + \rho g \sin \theta, \quad (1)$$

$$0 = -\frac{\partial \sigma_{yy}}{\partial y} - \rho g \cos \theta. \quad (2)$$

Using the boundary conditions of zero shear stress and pressure at the free surface, and assuming a constant density ρ (i.e., constant solids fraction ϕ) across the layer, eqs. (1) and (2) can be integrated to obtain

$$\tau_{yx} = -\rho g (h - y) \sin \theta, \quad (3)$$

$$\sigma_{yy} = \rho g (h - y) \cos \theta. \quad (4)$$

The effective friction coefficient $\mu(I)$, defined as the ratio of the magnitude of shear stress $|\tau_{yx}|$ to the confining pressure P , i.e.,

$$\mu(I) = \frac{|\tau_{yx}|}{P} \quad (5)$$

is dependent only on the dimensionless inertial number I in the dense flow regime. Mandal *et al.* [27] have proposed a non-monotonic variation of the effective friction coefficient $\mu(I)$ as

$$\mu(I) = \mu_s + \frac{c_1 - c_2 I}{1 + I_0/I}, \quad (6)$$

where μ_s , I_0 , c_1 and c_2 are the model parameters. The solids fraction ϕ shows a power law variation with the inertial number I and is given as

$$\phi(I) = \phi_{max} - aI^\alpha, \quad (7)$$

where ϕ_{max} , a and α are the model parameters. Simulation results in this study show that the first normal stress difference $N_1 = \sigma_{xx} - \sigma_{yy}$ to the pressure P ratio as well as the second normal stress difference $N_2 = \sigma_{yy} - \sigma_{zz}$ to the pressure P ratio are a function of inertial number I , i.e., $\frac{N_1}{P} = f_1(I)$, and $\frac{N_2}{P} = f_2(I)$ where $P = (\sigma_{xx} + \sigma_{yy} + \sigma_{zz})/3$ is the trace of the stress tensor. These functional forms can be used to relate the pressure P with the first as well as second normal stress difference σ_{yy} as

$$P = \frac{\sigma_{yy}}{1 + \frac{f_2(I) - f_1(I)}{3}}. \quad (8)$$

Using Eq. (4) we obtain,

$$P = \frac{\rho g(h - y) \cos \theta}{1 + \frac{f_2(I) - f_1(I)}{3}}. \quad (9)$$

Using the expression for inertial number $I = \frac{d\dot{\gamma}}{\sqrt{P/\rho_p}}$ with $\dot{\gamma} = \frac{dv_x}{dy}$ and rearranging, we get

$$\frac{dv_x}{dy} = \frac{I\sqrt{P/\rho_p}}{d}. \quad (10)$$

Using Eq. (9), Eq. (10) can be integrated to obtain the velocity in the x -direction as

$$v_x = v_{slip} + \frac{2I}{3d} \sqrt{\frac{\phi g \cos \theta}{1 + \frac{f_2(I) - f_1(I)}{3}}} \left[h^{3/2} - (h - y)^{3/2} \right], \quad (11)$$

where v_{slip} is the slip velocity at the base. Using Eqs. (3) and (9) in Eq. (5), the effective friction coefficient μ at any inclination θ is obtained as

$$\mu(I) = \frac{\tan \theta}{1 + \frac{f_2(I) - f_1(I)}{3}}. \quad (12)$$

Using our simulation data over a large range of I , we find that $f_1(I)$ shows a linear variation for the range of the inertial number considered in this study. We also find that $f_2(I)$ shows a quadratic variation with the inertial number. Thus we can express $f_1(I) = AI + B$ and $f_2(I) = CI^2 + DI + E$ for the range of inertial number of our interest. Using Eq. (6) along with the linear form of $f_1(I)$ and quadratic form of $f_2(I)$ in Eq. (12), we obtain an algebraic equation $G(I) = A_0I^3 + B_0I^2 + C_0I + D_0 = 0$.

This algebraic equation needs to be solved to obtain the value of the inertial number at a given inclination θ .

By using $f_1(I) = AI + B$ and $f_2(I) = CI^2 + DI + E$, we get the coefficients of the cubic equation as $A_0 = -C \tan \theta$, $B_0 = (A - D - CI_0) \tan \theta - c_2$, $C_0 = (-3 + B - E + AI_0 - DI_0) \tan \theta + 3\mu_s + 3\mu_m$ and $D_0 = ((-3 + B - E) \tan \theta + 3\mu_s)I_0$.

Solving the cubic equation $G(I) = 0$, we obtain three different possible values of inertial number I for a particular inclination θ . Only one of these values is found to be realistic. Using this value of the inertial number I for a given inclination angle θ , the solids fraction ϕ is obtained using Eq. (7). With the increase in the inclination angle θ , the inertial number I increases, and solids fraction ϕ decreases leading to an increase in the overall height of the flowing layer. This increased flowing layer height H at any inclination θ can be calculated from the mass balance over the entire layer using the following equation

$$H = H_{min} \phi_{max} / \phi, \quad (13)$$

where H_{min} is the minimum height of the static layer having maximum solids fraction ϕ_{max} . This value of H is used to get the velocity $v_x(y)$ using Eq. 11

IV. RESULTS AND DISCUSSION

We present DEM simulation results for the flow of spheres over a bumpy inclined surface starting from two different settled layer heights of $L_y = 20d$ and $L_y = 40d$ for restitution coefficient $e_n = 0.5$ where d is the mean particle diameter. All the quantities reported are non-dimensionalized using d , m , $\sqrt{d/g}$ and mg as length, mass, time, and force units respectively where m is the mass of the particle having diameter d and g is the gravitational acceleration.

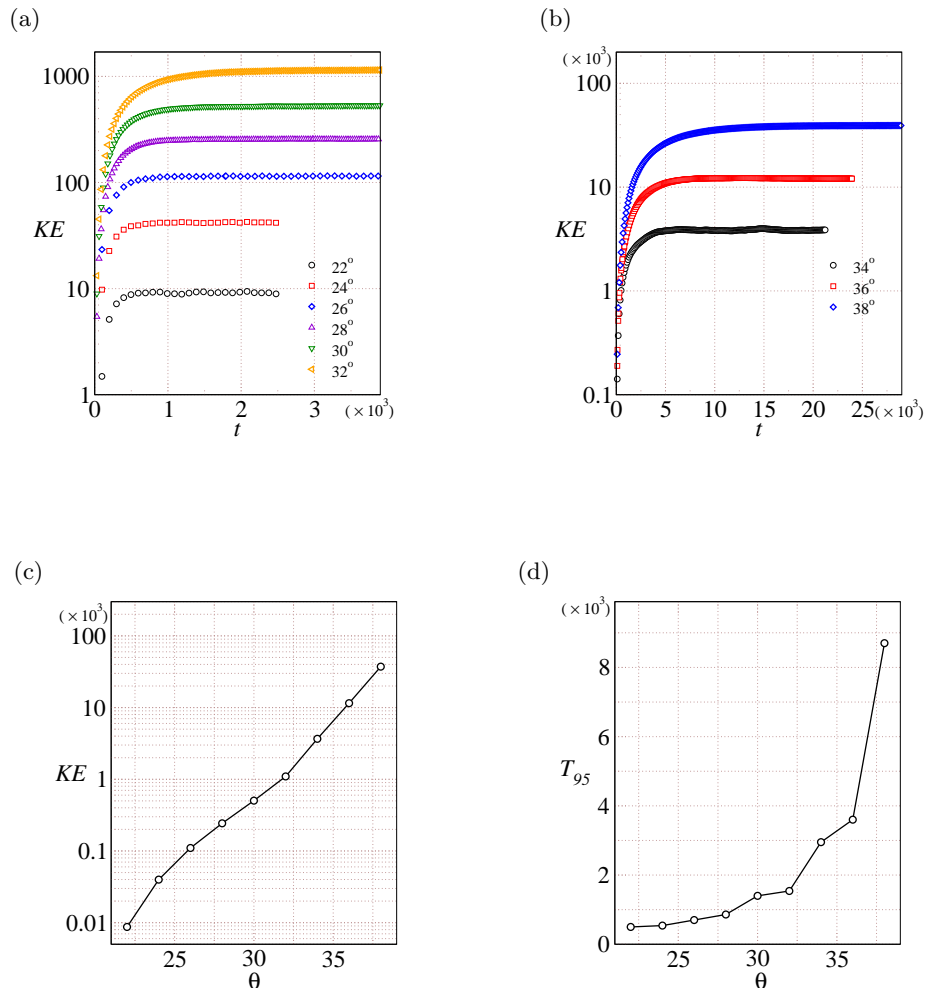


FIG. 3. Variation of the average kinetic energy KE with time t for (a) inclination angles $\theta \leq 32^\circ$ and (b) inclination angles $\theta > 32^\circ$. Variation of (c) steady-state kinetic energy and (d) time taken to reach 95% of steady-state kinetic energy with the inclination angle for $e_n = 0.5$.

We perform DEM simulations for inelastic spheres having restitution coefficient $e_n = 0.5$ spanning a wide range of inclination angles $\theta = 22^\circ$ to 38° for the initial flowing layer thickness $L_y = 40d$. The average kinetic energy of the particles at these inclinations are shown in Fig. 3(a) and Fig. 3(b). The average value of the kinetic energy keeps increasing with time and eventually becomes constant, indicating that the system is able to achieve a steady state at these inclinations. The average kinetic energy of the particles, shown in Fig. 3(a) and Fig. 3(b), becomes constant for all the inclination angles considered. This confirms that steady, fully developed flows are possible over a larger range of inclinations for $e_n = 0.5$. The average kinetic energy of the particles at steady state is plotted with the inclination angle in Fig. 3(c). As expected, the kinetic energy increases with inclination. A linear increase in the average kinetic energy is observed with the inclination angle θ . Fig. 3(d) shows the time taken to achieve 95% of steady state kinetic energy, denoted as T_{95} , for different inclinations. The time taken to reach a steady state increases with the inclination angle and a sharp change is observable after $\theta = 32^\circ$. Note that the kinetic energy in the y axis is non-dimensionalized using mgd where m is the mass, d is the particle diameter and g is the acceleration due to gravity.

B. Rheological model

From the DEM simulations data obtained from two different flowing layer thicknesses $L_y = 40d$ and $L_y = 20d$, we report the variation of the effective friction coefficient μ , solids fraction ϕ , the ratio of first normal stress difference to

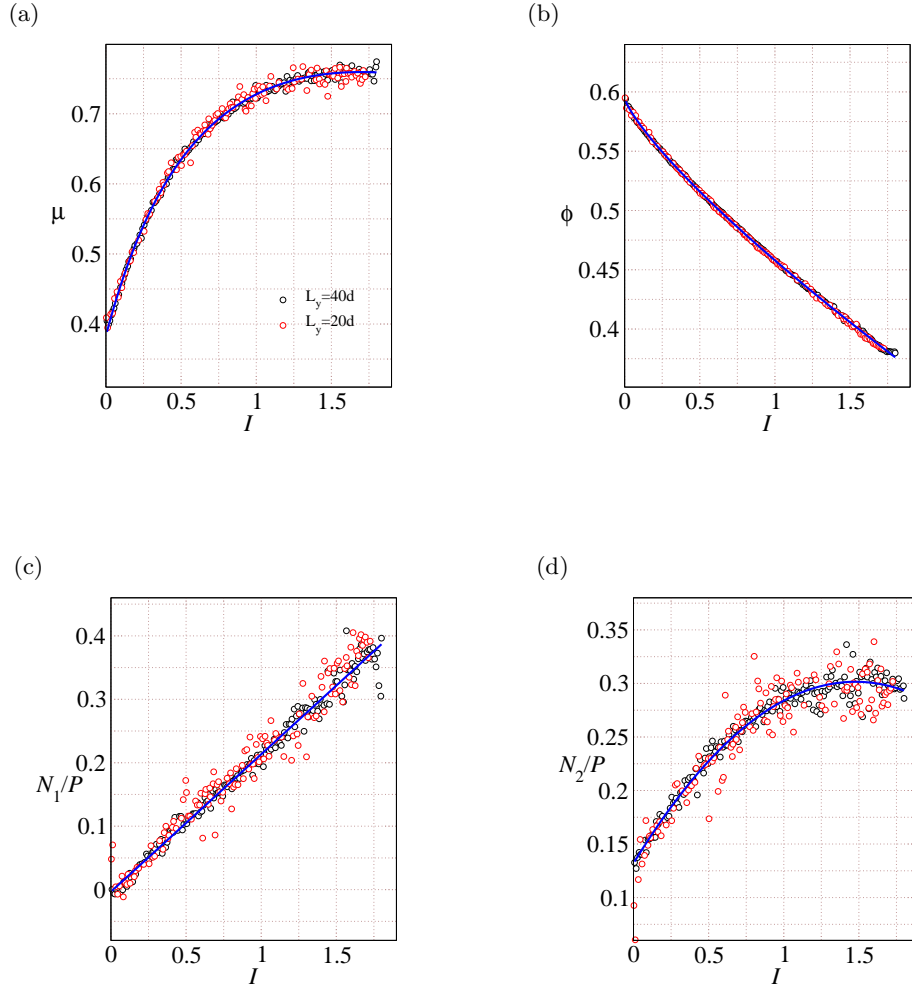


FIG. 4. Variation of the effective friction coefficient μ , solids fraction ϕ , first normal stress difference to the pressure ratio N_1/P , and second normal stress difference to the pressure ratio N_2/P with the inertial number I for $e_n = 0.5$. Symbols represent simulation data and lines represent best-fit curves. (a) Effective friction coefficient with best fit using Eq. (6) (solid line). (b) Solids fraction with best fit using Eq. (7). (c) First normal stress difference to the pressure ratio (symbols), with the best fit (line). Data for the entire range of I are fitted using $f_1(I) = AI + B$. (d) Second normal stress difference to the pressure ratio (symbols), with the best fit (line). Data for the entire range of I are fitted using $f_2(I) = CI^2 + DI + E$. Black circles correspond to the DEM simulations starting from a settled layer height of $L_y = 40d$ and red circles correspond to the DEM simulations starting from a settled layer height of $L_y = 20d$. The black solid lines represent the best fit to the DEM data using appropriate equations (See text for details).

pressure N_1/P and the ratio of second normal stress difference to pressure N_2/P with inertial number I for $e_n = 0.5$ in Fig. 4. The black circles correspond to the DEM simulations starting from a settled layer height of $L_y = 40d$ and the red circles correspond to the DEM simulations starting from a settled layer height of $L_y = 20d$. The data for the two cases do not differ significantly from each other and can be described using a single curve. The black solid line represents the best fit to the data accounting for both layer heights. The effective friction coefficient obtained from the simulations (shown using black and red symbols in Fig. 4(a)) increases up to $I \approx 1.8$ and shows a saturating behavior at large inertial numbers. There is a slight decrease in the effective friction coefficient μ at large inertial numbers I , however, the decrease is not prominent, and the inclusion of $\mu - I$ data for inclination angles $\theta > 38^\circ$ is needed to confirm the decrease in the effective friction coefficient at large inertial numbers. Given the sharp increase in the computational time for higher inclinations, we proceed with the analysis of the existing data.

Fitting the 4-parameter MK model using Eq. (6) to the simulation data shown in Fig. 4(a) indicates that the MK model (shown using solid lines) is able to describe the $\mu - I$ variation very well. Note that the simulation data for the inclination angle $\theta = 22^\circ - 38^\circ$ is considered to obtain the model parameters. The MK model parameters are reported in Table I. The variation of solids fraction is plotted with the inertial number in Fig. 4(b). The solid line shown in Fig. 4(b) is obtained by fitting the power law variation of ϕ with I (Eq. (7)) to the simulation data. The

dilatancy law model parameters are reported in Table II. In Fig. 4(c), we report the variation of the ratio of the first normal stress difference to the pressure ratio N_1/P with the inertial number I . The variation for the first normal stress difference to the pressure ratio N_1/P with the inertial number I is described well by a linear relation of the form $N_1/P = f_1(I) = AI + B$. The first normal stress difference law model parameters are reported in Table III. We also report the variation of the ratio of the second normal stress difference to the pressure ratio N_2/P with the inertial number I . The variation for the second normal stress difference to the pressure ratio N_2/P with the inertial number I is described well by a quadratic relation of the form $N_2/P = f_2(I) = FI^2 + GI + H$. The second normal stress difference law model parameters are reported in Table IV. A comparison of Fig. 4(c) and Fig. 4(d) shows that while N_1/P is zero at low inertial numbers, N_2/P is found to be positive even for the quasistatic systems with $I \sim 0$. In addition, $N_2/P > N_1/P$ for $I \leq 1.25$. For $I > 1.25$, however, N_1/P becomes larger than N_2/P . This transition of $N_2/P - N_1/P$ from positive to negative at $I \sim 1.25$ needs to be explored further.

TABLE I. Model parameters for MK model

e_n	μ_s	c_1	c_2	I'_0
0.5	0.383	0.821	0.131	1.002

TABLE II. Model parameters for dilatancy power law

e_n	ϕ_{max}	a	α
0.5	0.595	0.137	0.797

TABLE III. Model parameters for linear $N_1/P = AI + B$.

e_n	A	B
0.5	0.217	-0.003

C. Theoretical predictions

Using the rheological model parameters given in Table I-IV, we predict various flow properties of interest. These theoretical predictions are reported as solid lines in Figs. 5 and 6. The velocity profiles predicted using the theory are found to be in excellent agreement with the simulation results for inclination angles ranging from $\theta = 22^\circ - 32^\circ$ (see Fig. 5(a)). The slip velocity, which appears to be small for these inclinations is taken from the simulation data. The predicted values of the solids fraction ϕ are also found to be in very good agreement for inclination angles $\theta = 22^\circ$ to $\theta = 32^\circ$ as shown in Fig. 5(b). The theoretical inertial numbers are also found to be in good agreement with the inertial numbers obtained from DEM simulations (see Fig.6(c)).

Figs.6(a-d) shows the comparison between DEM simulations and the theoretical predictions for the pressure P , shear stress τ_{yx} , first normal stress difference N_1 , and the second normal stress difference N_2 for the range of inclinations $\theta = 22^\circ$ to $\theta = 32^\circ$. The theoretical predictions using the rheological parameters are in very good agreement with the DEM simulation results. Comparison of N_1 and N_2 shows that N_2 is higher than N_1 for these range of inclinations.

We next use the rheological model parameters given in Table I-IV to predict various flow properties at large inclination angles ranging from $\theta = 34^\circ - 38^\circ$. These theoretical predictions are reported as solid lines in Figs. 7 and 8. The velocity profiles predicted using the theory are found to be in good agreement with the simulation results even at large inclination angles ranging from $\theta = 34^\circ - 38^\circ$ (see Fig. 7(a)). We use the slip velocity obtained from DEM simulations in the theoretical predictions. The predicted values of the solids fraction ϕ are also found to be in very good agreement for inclination angles $\theta = 34^\circ$ to $\theta = 38^\circ$ as shown in Fig. 7(b). In addition, the theoretical inertial numbers are also found to be in good agreement with the inertial numbers obtained from DEM simulations (see Fig.8(c)) except the largest inclination angle $\theta = 38^\circ$ where the theory predicts the inertial number $I = 1.76$ in comparison to the inertial number $I = 1.9$ obtained from DEM simulations. Figs. 8(a)-(d) show the comparison between DEM simulations and the theoretical predictions for the pressure P , shear stress τ_{yx} , first normal stress difference N_1 , and the second normal stress difference N_2 for the large inclinations angles ranging from $\theta = 34^\circ$ to

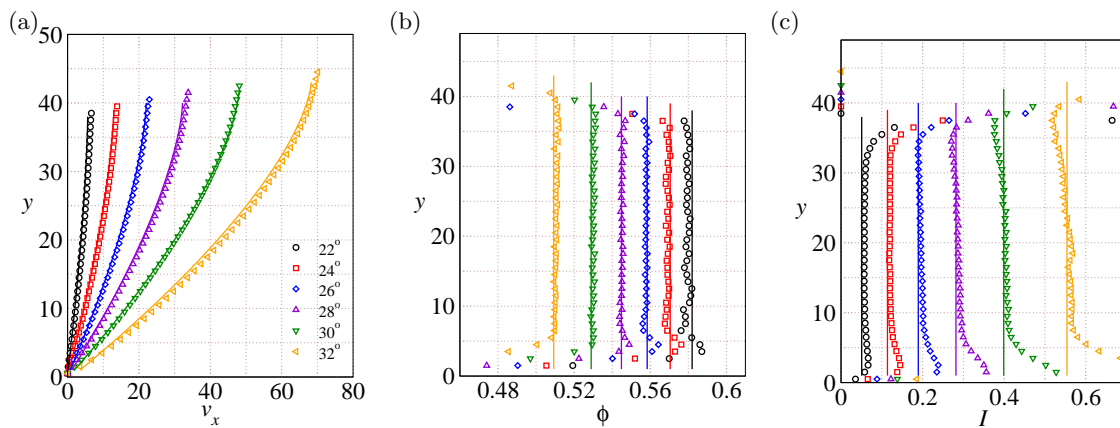


FIG. 5. Variation of the (a) velocity v_x , (b) solids fraction ϕ , and (c) inertial number I across the layer y at inclination angles $\theta = 22^\circ - 32^\circ$. All data correspond to $e_n = 0.5$. Solid lines represent the theoretical predictions (see text for details). The height of the settled layer at $t = 0$ is $40d$.

TABLE IV. Model parameters for quadratic $N_2/P = FI^2 + GI + H$

e_n	F	G	H
0.5	-0.078	0.23	0.132

$\theta = 38^\circ$. The theoretical predictions using the rheological parameters are in very good agreement with the DEM simulation results.

Many industrial granular flows in conveyors and chutes have flowing layer thickness in the range $10d - 20d$. It is well known that the inertial number I and solids fraction ϕ are nearly constant in the bulk region of the flowing layer of chute flow for any given inclination angle θ . The bulk region is defined as the region that is away from the base of the chute and the free surface. The bulk region is very important in order to estimate the rheological properties. Lack of bulk region in the case of low flowing layer thickness will lead to fluctuations of flow properties in the bulk and will lead to significant errors in estimating the rheological parameters. Due to the lack of bulk region in the case of low flowing layer thickness $L_y = 20d$, we have performed DEM simulations starting from a settled flowing layer height $L_y = 40d$. We will now use the rheological model parameters given in Table I-IV obtained from the flowing layer thickness $L_y = 40d$ to predict various flow properties for a wider range of inclination angles ranging from $\theta = 22^\circ - 38^\circ$ for low flowing layer thickness $L_y = 20d$ which is the initial settled flowing layer thickness.

These theoretical predictions are reported as solid lines in Figs. 9 and 10. The velocity profiles predicted using the theory are found to be in good agreement with the simulation results for inclination angles ranging from $\theta = 22^\circ - 32^\circ$ (see Fig. 9(a)). Figs. 9(b) and Fig. 9(c) show that the predicted values of the solids fraction ϕ and inertial number I are also found to be in very good agreement for inclination angles $\theta = 22^\circ$ to $\theta = 32^\circ$. Figs.10(a-d) shows the comparison between DEM simulations and the theoretical predictions for the pressure P , shear stress τ_{yx} , first normal stress difference N_1 , and the second normal stress difference N_2 for inclinations angles ranging from $\theta = 22^\circ$ to $\theta = 32^\circ$. Again, the theoretical predictions using the rheological parameters are in very good agreement with the DEM simulation results. Next, the theoretical predictions for the various flow properties of interest have been compared with the DEM simulation results for higher inclination angles in the range of $\theta = 34^\circ$ to $\theta = 38^\circ$. The predictions from the rheological parameters obtained using the simulations data of $L_y = 40d$ layer are in very good agreement with the DEM simulation results for low flowing layer thickness $L_y = 20d$ suggesting that rheological parameters obtained from large flowing layer thickness data can be used to predict the flow properties for low flowing layer thickness as well (shown in Figs.11-12).

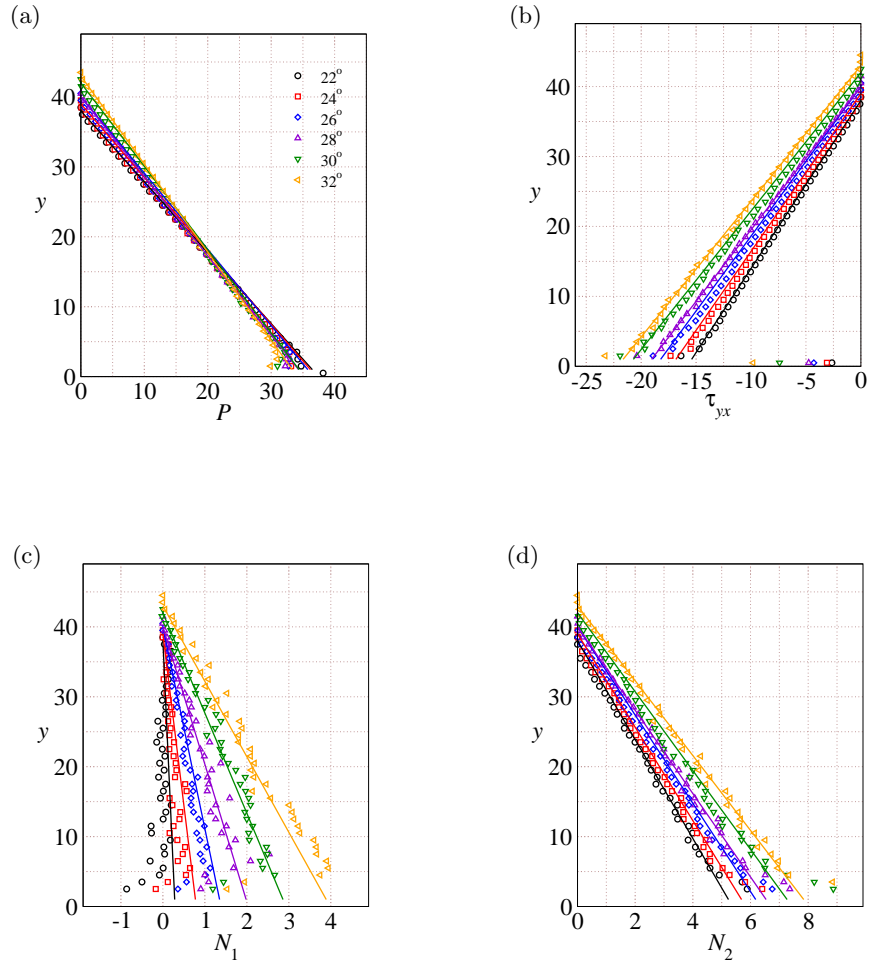


FIG. 6. Variation of the (a) pressure P , (b) shear stress τ_{yx} (c) first normal stress difference N_1 and (d) second normal stress difference N_2 across the layer y at inclination angles $\theta = 22^\circ - 32^\circ$. All data correspond to $e_n = 0.5$. Solid lines represent the theoretical predictions (see text for details). The height of the settled layer at $t = 0$ is $40d$.

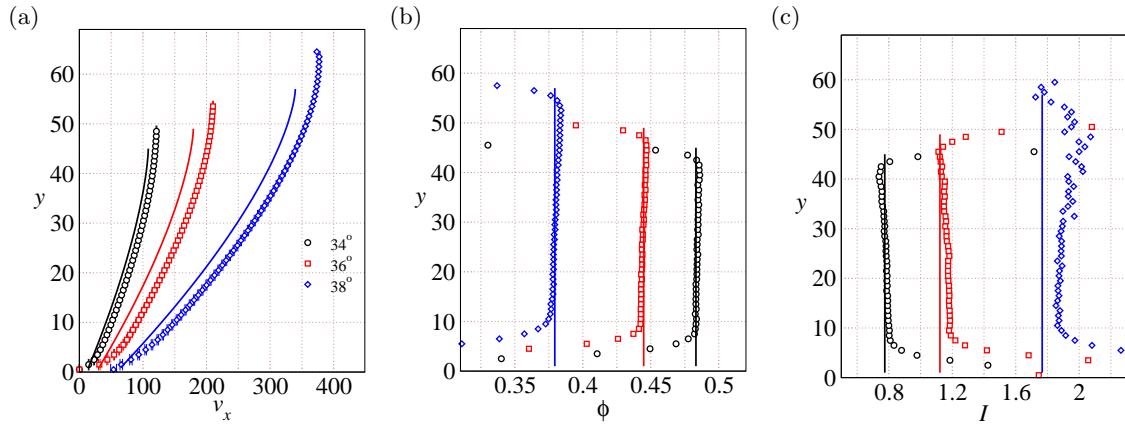


FIG. 7. Variation of the (a) velocity v_x , (b) solids fraction ϕ , and (c) inertial number I across the layer y at inclination angles $\theta = 34^\circ - 38^\circ$. All data correspond to $e_n = 0.5$. Solid lines represent the theoretical predictions (see text for details). The height of the settled layer at $t = 0$ is $40d$.

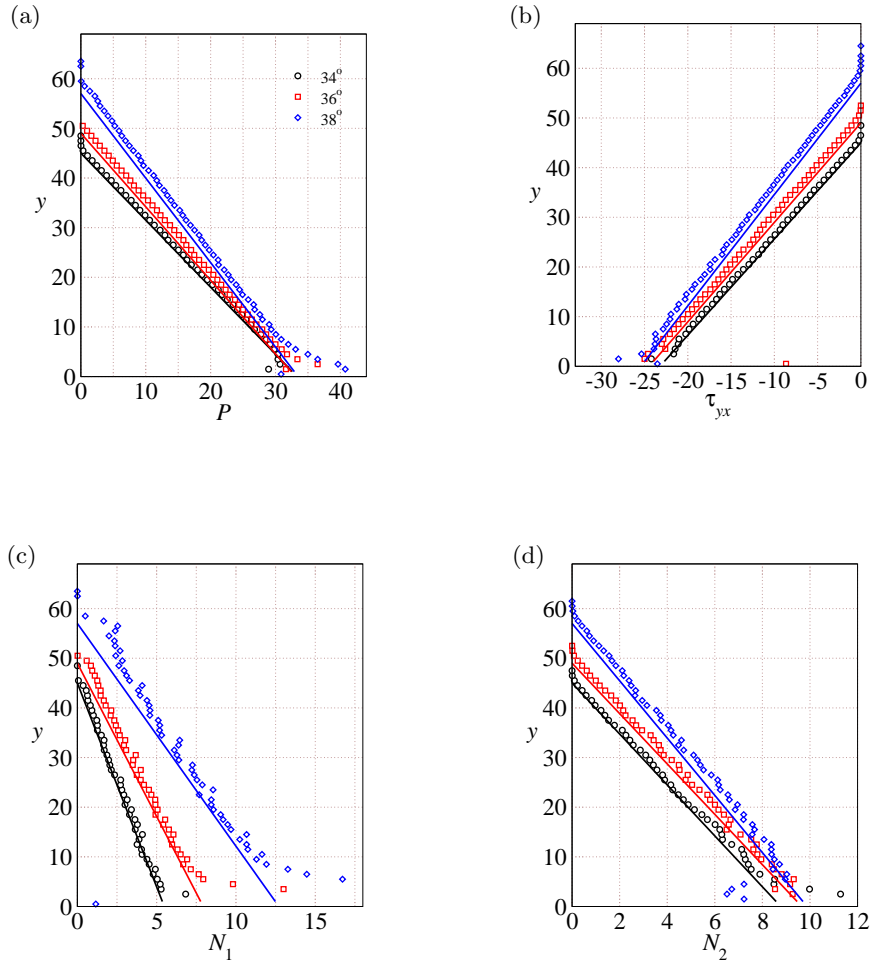


FIG. 8. Variation of the (a) pressure P , (b) shear stress τ_{yx} (c) first normal stress difference N_1 and (d) second normal stress difference N_2 across the layer y at inclination angles $\theta = 34^\circ - 38^\circ$. All data correspond to $e_n = 0.5$. Solid lines represent the theoretical predictions (see text for details). The height of the settled layer at $t = 0$ is $40d$.

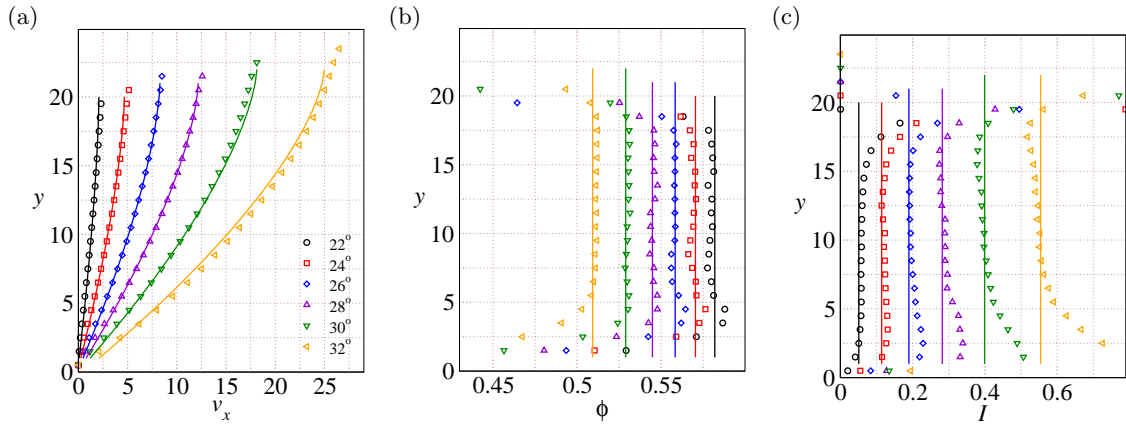


FIG. 9. Variation of the (a) velocity v_x , (b) solids fraction ϕ , and (c) inertial number I across the layer y for inclination angles ranging from $\theta = 22^\circ$ to $\theta = 32^\circ$ for $20d$ thickness of the layer. All data correspond to $e_n = 0.5$. Solid lines represent the theoretical predictions using the model parameters obtained from DEM simulation data.

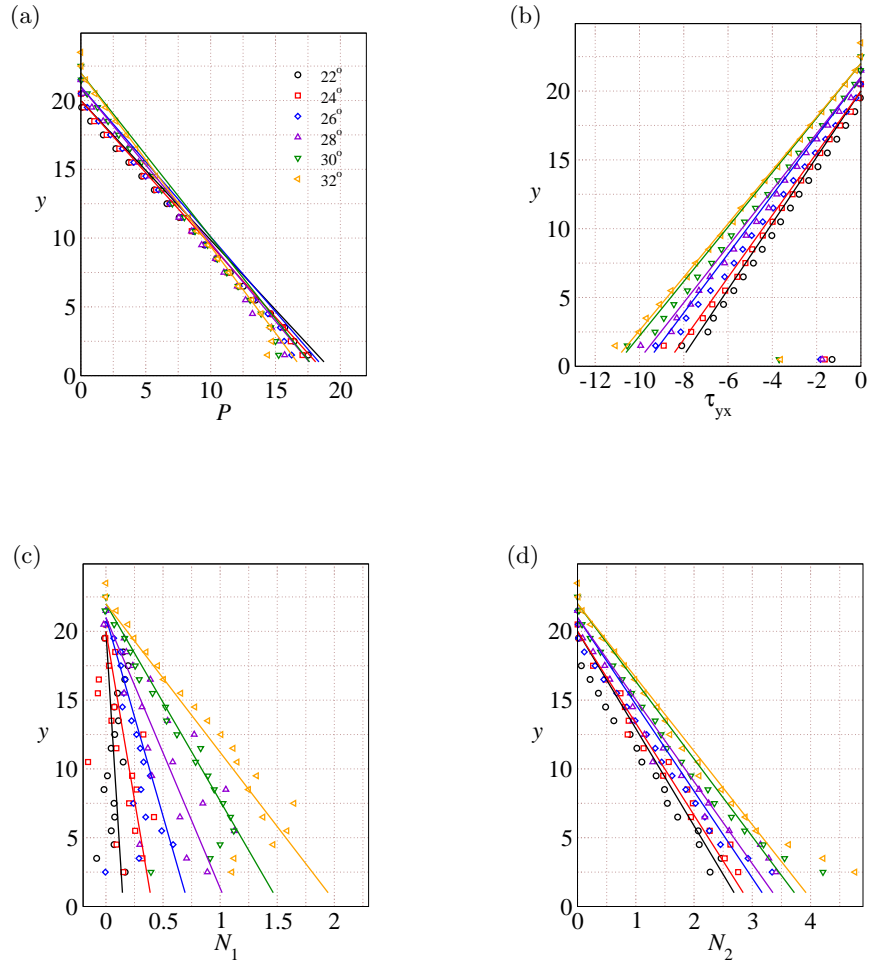


FIG. 10. Variation of the (a) pressure P , (b) shear stress τ_{yx} (c) first normal stress difference N_1 and (d) second normal stress difference N_2 across the layer y for inclination angles ranging from $\theta = 22^\circ$ to $\theta = 32^\circ$. All data correspond to $e_n = 0.5$. Solid lines represent the theoretical predictions using the model parameters obtained from DEM simulations data.

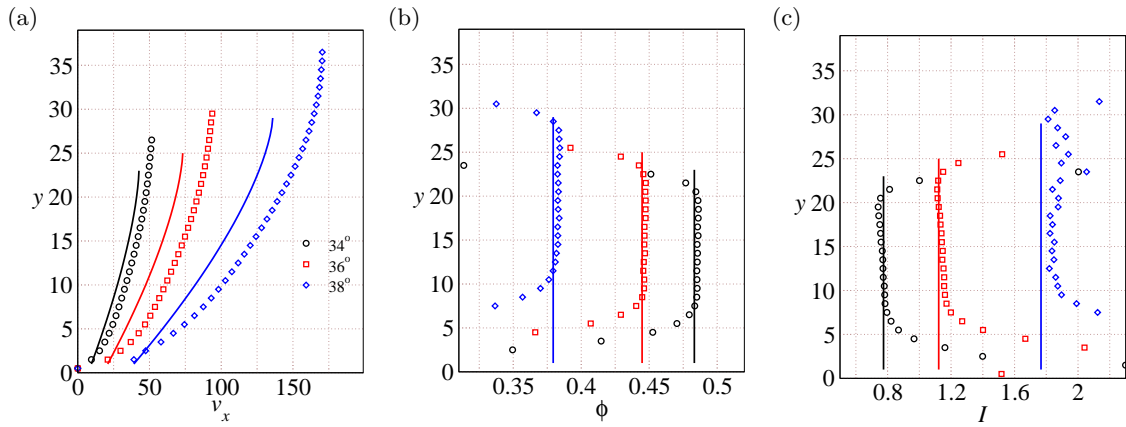


FIG. 11. Variation of the (a) velocity v_x , (b) solids fraction ϕ , and (c) inertial number I across the layer y for inclination angles ranging from $\theta = 34^\circ$ to $\theta = 38^\circ$. All data correspond to $e_n = 0.5$. Solid lines represent the theoretical predictions using the model parameters obtained from DEM simulations data of $L_y = 40d$ layer thickness.

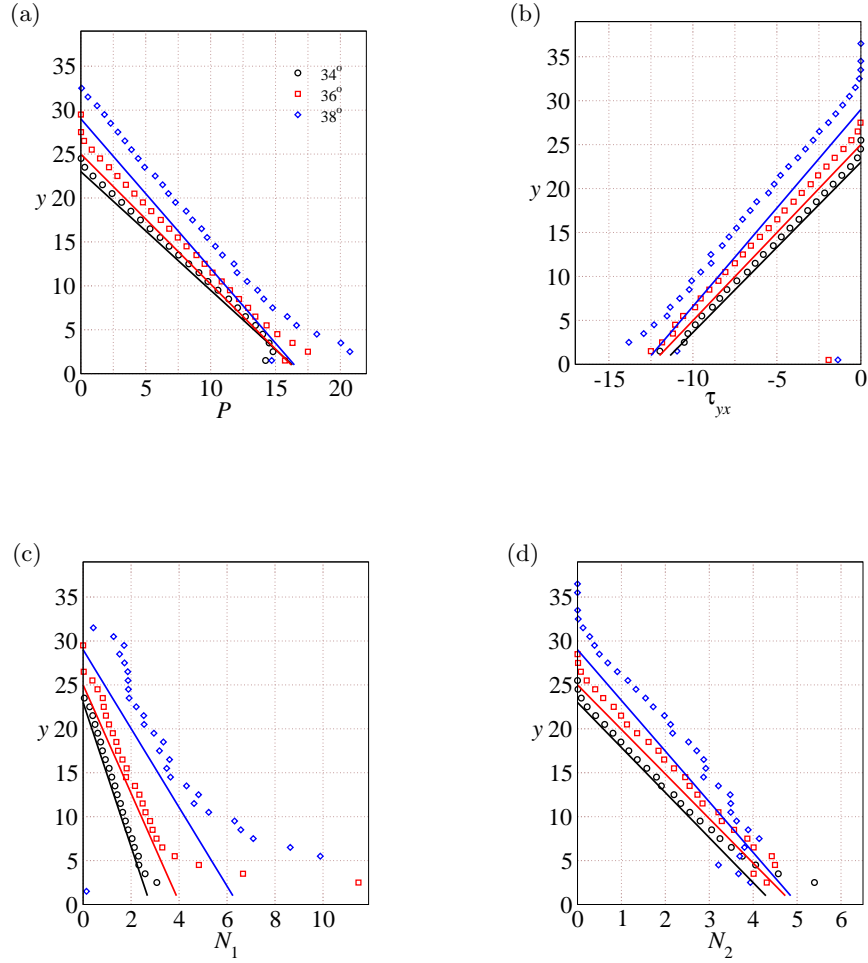


FIG. 12. Variation of the (a) pressure P , (b) shear stress τ_{yx} (c) first normal stress difference N_1 and (d) second normal stress difference N_2 across the layer y for inclination angles ranging from $\theta = 34^\circ$ to $\theta = 38^\circ$. All data correspond to $e_n = 0.5$. Solid lines represent the theoretical predictions using the model parameters obtained from DEM simulations data of $L_y = 40d$ layer thickness.

D. Bulk average properties

Figs. 13(a)-13(d) summarise the results over the entire range of inclinations investigated in this study and show the variation of the inertial number I_{bulk} , solids fraction ϕ_{bulk} , height of the bulk region of the flowing layer h_{bulk} and the slip velocity at the base v_{slip} as a function of inclination angle θ for restitution coefficient $e_n = 0.5$. The slope of the curve for the lower angles differs significantly from that for the higher angles. This slope contrast is evident in the case of slip velocity shown in Fig. 13 for different flow regimes: dense flows with negligible slip velocity at lower angles and rapid, dilute flows with large slip velocities at higher angles. The steady-state solids fraction ϕ is found to decrease with the increase in the inclination angle θ and can be seen in Fig. 13(b). The decrease in the solids fraction is followed by the dilation of the bulk flowing layer thickness $h_{bulk} = h_{initial} \times \phi_{max} / \phi_{steady}$ which increases with the inclination angle. This increase in the bulk flowing layer thickness with the inclination angle is shown in Figs. 13(c). The slip velocity at the base of the chute is shown in Figs. 13(d) which increases with the increase in inclination angle and changes its slope gradually beyond inclination angle $\theta = 30^\circ$.

E. Role of normal stress difference

In this section, we will discuss the effect of the first and the second normal stress differences on the flow properties of granular materials for the range of inclination angle $\theta = 22^\circ$ to $\theta = 32^\circ$. Figure 14(a) shows the theoretical predictions of the inertial number using the JFP model with and without considering the effect of the first and the second normal

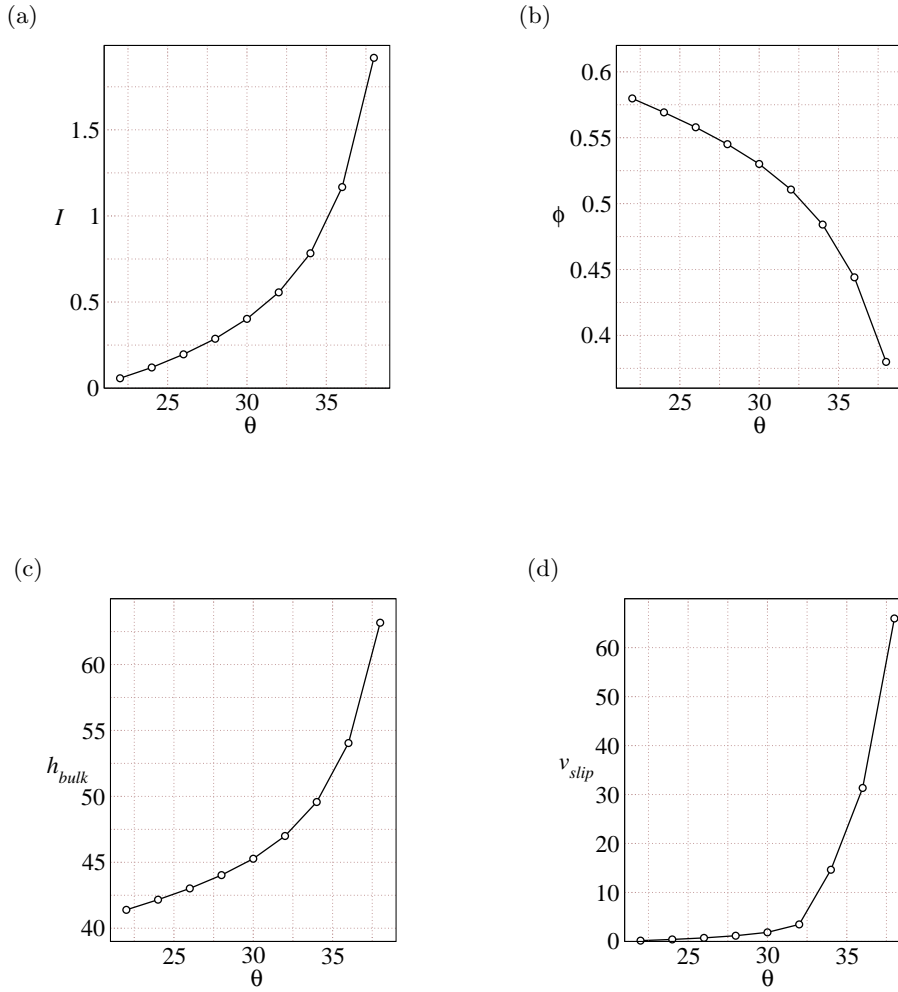


FIG. 13. Variation of (a) inertial number I , (b) solids fraction ϕ , (c) bulk layer height H_{bulk} and (d) slip velocity v_{slip} with inclination angle θ for restitution coefficient $e_n = 0.5$.

stress differences i.e. by assuming $f_1(I) = N_1/P = 0$ and $f_2(I) = N_2/P = 0$ in the latter case. Symbols represent the DEM simulation results. The dashed lines correspond to the theoretical predictions of the inertial number I using the JFP model where the normal stress differences have been ignored whereas the solid lines correspond to the theoretical predictions of the inertial number I using the JFP model where the normal stress differences have been considered. It is evident from figure 14(a) that the theoretical inertial number starts to deviate from the DEM simulation results as we increase the inclination angle θ . Figure 14(b) shows the theoretical predictions of the inertial number using the modified rheological model with and without considering the effect of the first and the second normal state differences. The latter case assumes $f_1(I) = N_1/P = 0$ and $f_2(I) = N_2/P = 0$. As before, symbols represent the DEM simulation results. The dashed lines correspond to the theoretical predictions of the inertial number I using the modified rheological model where the normal stress differences have been ignored whereas the solid lines correspond to the theoretical predictions of the inertial number I using the modified rheological model where the normal stress differences have been considered. The deviation in the theoretical predictions of the inertial number I from the DEM simulation results are observed in the case of the modified rheological model as well and this deviation is more significant at higher inclinations. These results suggest that the role of the normal stress differences becomes crucial not only for large inclinations but also for small inclinations as well and one must consider these effects in order to accurately predict the flow properties. Neglecting the effect of the normal stress differences will lead to significant errors in the theoretical predictions.

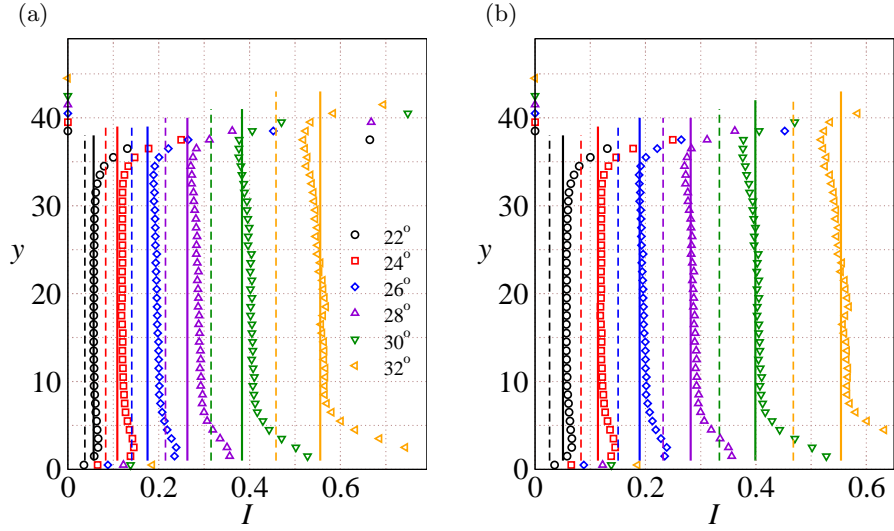


FIG. 14. Theoretical predictions of the inertial numbers using the a) JFP model, and b) modified rheological model with and without the effect of normal stress differences and its comparison with the DEM simulation results for inclination angles $\theta = 22^\circ$ to $\theta = 32^\circ$ of the inertial number predictions of the

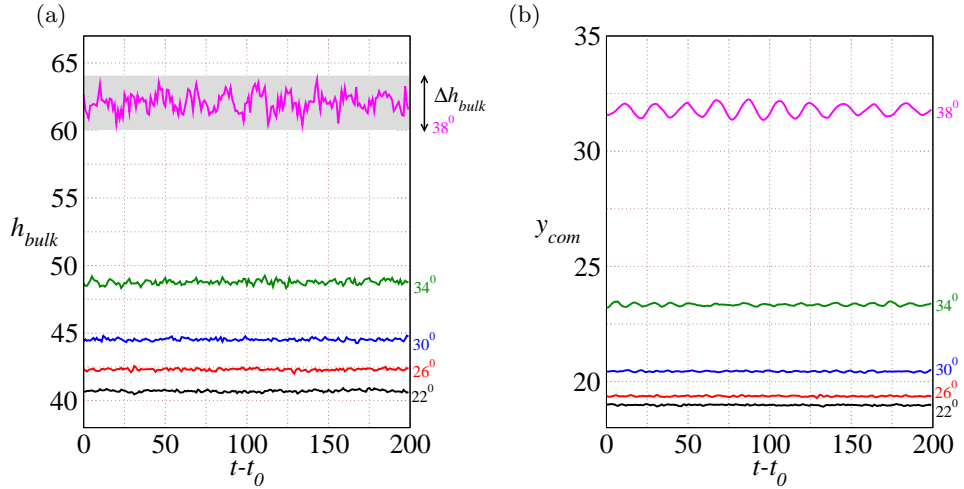


FIG. 15. Steady state oscillating behavior of a) bulk flowing layer thickness h_{bulk} and b) center of mass y_{com} at different inclinations for restitution coefficient $e_n = 0.5$.

F. Oscillations in the steady flow

The steady-state oscillations in the bulk layer height h_{bulk} are shown in Fig. 15(a) over a time period of 200 time units starting from a time instant t_0 . Oscillations in the center of mass y_{com} are shown in Fig. 15(b). These height measurements are done after the flow has achieved steady kinetic energy (hence t_0 varies with the inclination angle θ). The oscillations in the bulk layer height h_{bulk} as well as center of mass y_{com} keep increasing with the inclination angle. While the difference between maximum and minimum bulk height is less than the particle diameter for inclinations $\theta \leq 30^\circ$, this variation becomes $\Delta h_{bulk} \approx 4d$ for $\theta = 38^\circ$ case (Fig. 15(a)). These oscillations indicate that the role of density and height variations become important and cannot be ignored for granular flows at inertial numbers

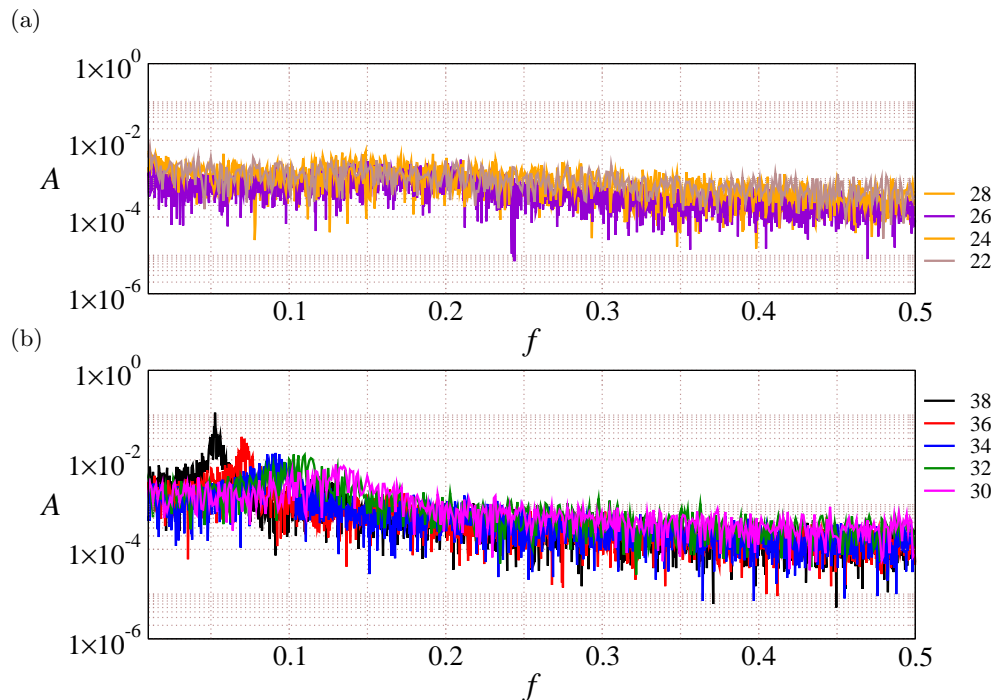


FIG. 16. Fast Fourier transform analysis of the center of mass data for a) low to moderate inclination angles ranging from $\theta = 22^\circ$ to $\theta = 28^\circ$, b) moderate to large inclination angles ranging from $\theta = 30^\circ$ to $\theta = 38^\circ$.

comparable to unity.

In order to investigate the time-periodic behavior of the layer at high inertial numbers, we performed a Fast Fourier Transform (FFT) analysis of the time series data of the center of mass position at steady state. Figure 16 shows the amplitude spectrum of the center of mass for different inclinations. The amplitude spectrum for inclinations $\theta = 22^\circ$ to $\theta = 28^\circ$ shows nearly uniform distribution for all frequencies as shown in Fig. 16(a). At higher inclinations, a dominant frequency with a clear peak starts to appear and is shown in Fig. 16(b). The occurrence of a dominant frequency in the amplitude spectrum confirms that the variation of layer height occurs with a characteristic time period at these large inclinations. The peak frequency keeps moving to lower values as the inclination angle increases, indicating that the time period of oscillations increases with the inclination angle. Figure 16(b) also shows that the amplitude of oscillations at the $\theta = 38^\circ$ is nearly an order of magnitude higher compared to those at $\theta = 30^\circ$.

FFT analysis of the bulk layer height, center of mass, and kinetic energy data are shown for three different inclinations i.e. $\theta = 30^\circ$, $\theta = 34^\circ$, and $\theta = 38^\circ$ as shown in Fig. 17(a-c). The black solid line corresponds to the center of mass position, the red solid line corresponds to the bulk flowing layer thickness, and the black solid line corresponds to the kinetic energy. We find that the maximum amplitude of the spectrum is observed at the same frequency $f = 0.05$ for different properties at the inclination $\theta = 38^\circ$. For $\theta = 34^\circ$ and $\theta = 30^\circ$, the corresponding frequencies are $f = 0.09$ and $f = 0.13$ respectively. Hence we conclude that the oscillations at high inclinations affect these properties of the flow in a nearly identical fashion.

We also investigate the role of the simulation box size on the dominant frequency of oscillation and its corresponding amplitude. For this, we have considered three different simulation box size of base area $15d \times 15d$, $20d \times 20d$ and $30d \times 30d$ where d is the diameter of the . The initial height of the simulation setup at $t = 0$ for all the three cases is same i.e. $40d$. Fig. 18 shows the FFT analysis of the center of mass data at $\theta = 38^\circ$ for three different box sizes. We find that the maximum amplitude of the spectrum is observed at the same frequency $f = 0.05$ at the inclination $\theta = 38^\circ$ for three different simulation box size confirming that the amplitude and frequency of the oscillation is independent of the simulation box size.

V. RHEOLOGY AT LARGE INCLINATIONS

From the DEM simulations data obtained from the flowing layer thicknesses $L_y = 40d$, we report the variation of the effective friction coefficient μ , solids fraction ϕ , the ratio of first normal stress difference to pressure N_1/P and the

ratio of second normal stress difference to pressure N_2/P with inertial number I for $e_n = 0.5$ in Fig. 19. The different coloured symbols represents the curve for different inclinations. The effective friction coefficient obtained from the simulations (shown using different symbols in Fig. 19(a)) increases up to $I \approx 1.8$ and shows a sudden decrease at large inertial numbers. There was a slight decrease in the effective friction coefficient μ at large inertial numbers I reported at earlier sections upto the inclination angle $\theta = 38^\circ$, however, the decrease was not prominent. The inclusion of $\mu - I$ data for inclination angles $\theta > 38^\circ$ is shown to confirm the decrease in the effective friction coefficient at large inertial numbers.

VI. CONCLUSIONS

We perform three-dimensional DEM simulations of slightly polydisperse, frictional, inelastic spheres flowing down a bumpy inclined plane varying over a wide range of inclination angles. We have considered two different flowing layer thicknesses: a thin layer with a settled layer height of $L_y = 20d$ and a thick layer with a settled layer height of $L_y = 40d$. We are able to observe steady flows for inclinations up to $\theta = 38^\circ$ for $e_n = 0.5$. The steady flow observed at $\theta = 38^\circ$ corresponds to inertial number as high as $I \approx 1.9$ and solids fraction as low as $\phi \approx 0.38$. The flows at such high inertial numbers exhibit significant slip velocity at the bumpy base. However, they also exhibit a bulk core region with a nearly constant solids fraction as typically observed in case of dense flows. The solids fraction value in the bulk becomes as low as $\phi \approx 0.38$ and the height of the layer increases up to $70d$ starting from a settled layer height of $40d$ for the highest inclination angle $\theta = 38^\circ$ considered in this study.

Using the simulation data over a large range of inertial numbers, we find that key conclusions of the modified rheology previously reported for 2D systems in Patro *et al.* [32] are observable in 3D as well. Given the range of inclination angles $\theta = 22^\circ - 38^\circ$ considered in this study, we were unable to observe the decreasing part of the $\mu - I$ curve at large inertial numbers. The inclusion of higher angle data $\theta > 38^\circ$ may confirm the non-monotonic variation. However, even for this limited range of data, we find that the $\mu - I$ relation as per the modified rheological model does fit the data better compared to the JFP model. A power law relation describes the $\phi - I$ data well over the entire range of I . In addition, both the first and second normal stress difference laws, relating the normal stress differences to pressure ratio $f_1(I) = N_1/P$ and $f_2(I) = N_2/P$ with the inertial number I is also proposed. We show that these normal stress difference laws needs to be considered to describe the rheology for large values of inertial numbers. It

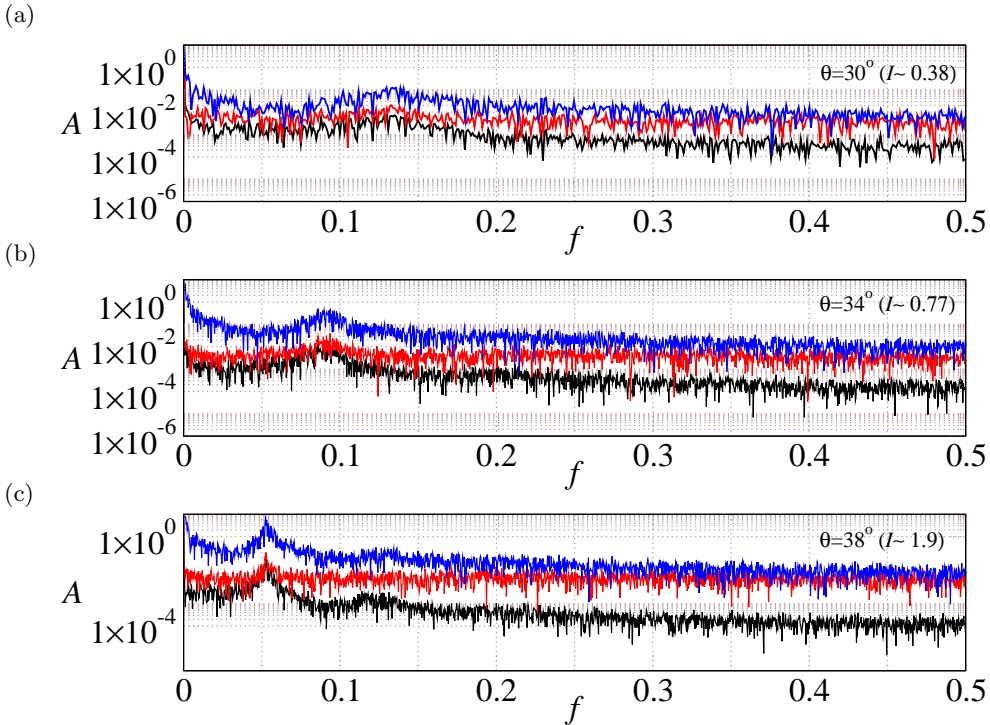


FIG. 17. Fast Fourier transform analysis of the center of mass (shown in black line), bulk flowing layer thickness (shown in red line) and kinetic energy (shown in blue line) for inclination angle a) $\theta = 30^\circ$, b) $\theta = 34^\circ$ and c) $\theta = 38^\circ$.

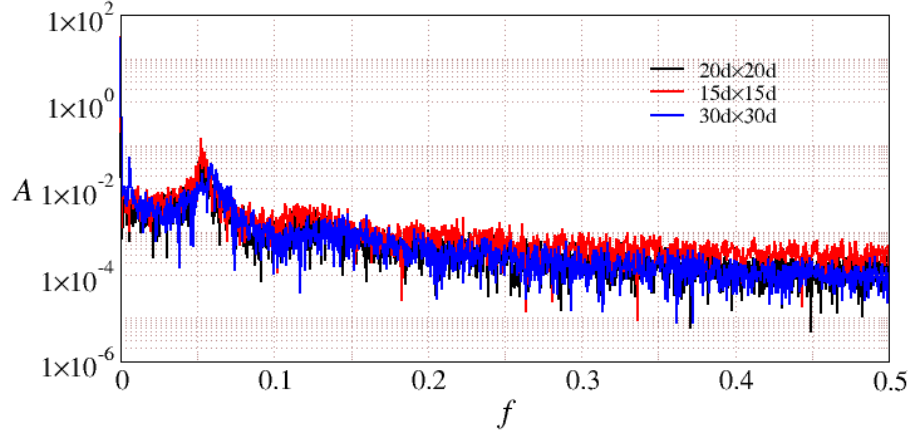


FIG. 18. Fast Fourier transform analysis of the center of mass data at $\theta = 38^\circ$ for three different simulation box sizes.

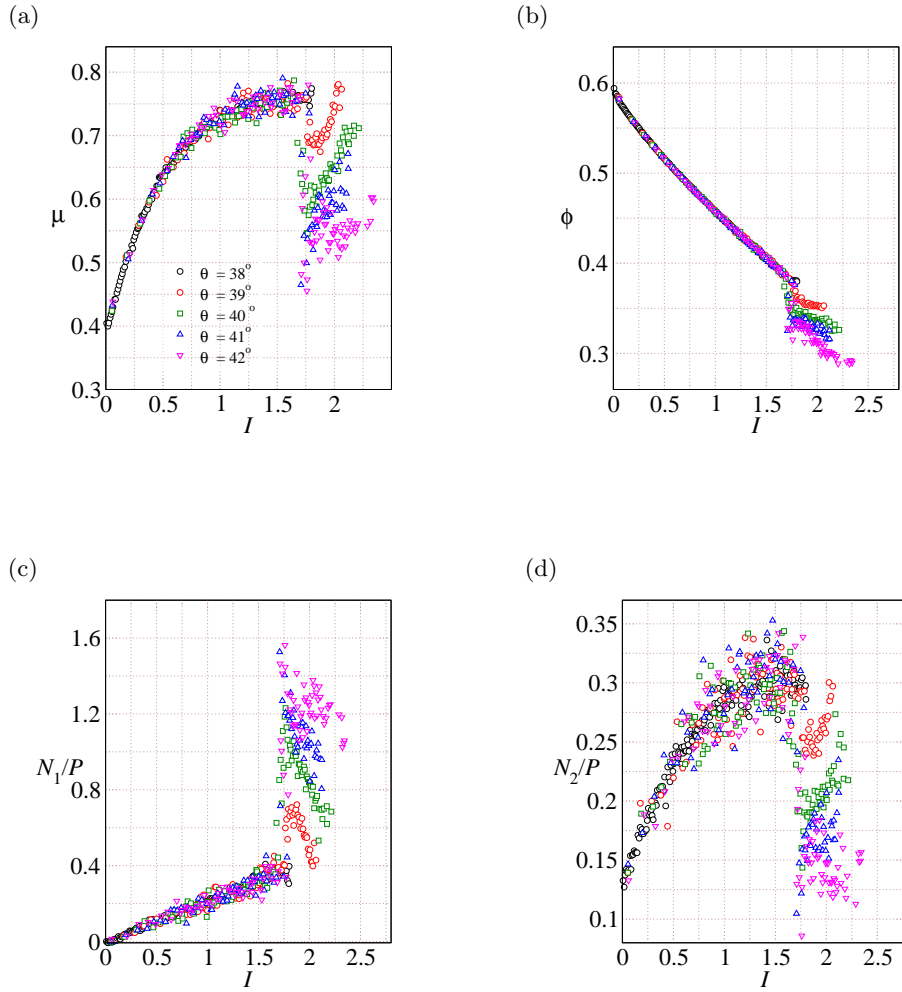


FIG. 19. Variation of (a) Effective friction coefficient μ , (b) solids fraction ϕ , (c) first normal stress difference to the pressure ratio N_1/P and (d) Second normal stress difference to the pressure ratio N_2/P with the inertial number I for inclination angles $\theta = 38^\circ - 42^\circ$ and for restitution coefficient $e_n = 0.5$.

is worth highlighting that the periodic oscillations in the flow properties at steady state become prominent at high inclinations. The bulk layer height, the center of mass position, and the kinetic energy show oscillations around the steady state value with a characteristic frequency beyond an inclination angle. The dominant frequency for all the properties at inclination $\theta = 38^\circ$ shows a peak around $f = 0.05$. We conclude that the modified form of the $\mu - I$ rheology using the MK model along with the dilatancy law and both the normal stress difference law is able to predict the flow behavior for most of the bulk layer and is in good agreement with the simulation results up to inclination angle $\theta = 38^\circ$.

ACKNOWLEDGEMENTS

AT gratefully acknowledges the financial support provided by the Indian Institute of Technology Kanpur via the initiation grant IITK/CHE/20130338.

DATA AVAILABILITY

The data that support the findings of this study are available from the corresponding author upon request.

REFERENCES

-
- [1] O. Pouliquen, Scaling laws in granular flows down rough inclined planes, *Phys. Fluids* **11**, 542 (1999).
 - [2] G. MiDi, On dense granular flows., *European Physical Journal E-Soft Matter* **14** (2004).
 - [3] P. Jop, Y. Forterre, and O. Pouliquen, Crucial role of sidewalls in granular surface flows: consequences for the rheology, *J. Fluid Mech.* **541**, 167 (2005).
 - [4] A. J. Holyoake and J. N. McElwaine, High-speed granular chute flows, *J. Fluid Mech.* **710**, 35 (2012).
 - [5] O. Pouliquen, On the shape of granular fronts down rough inclined planes, *Phys. Fluids* **11**, 1956 (1999).
 - [6] J. Heyman, P. Boltenhagen, R. Delannay, and A. Valance, Experimental investigation of high speed granular flows down inclines, in *EPJ Web of Conferences*, Vol. 140 (2017) p. 03057.
 - [7] E. L. Thompson and H. E. Huppert, Granular column collapses: further experimental results, *J. Fluid Mech.* **575**, 177 (2007).
 - [8] L. Lacaze, J. C. Phillips, and R. R. Kerswell, Planar collapse of a granular column: Experiments and discrete element simulations, *Phys. Fluids* **20**, 063302 (2008).
 - [9] G. Lube, H. E. Huppert, R. S. J. Sparks, and M. A. Hallworth, Axisymmetric collapses of granular columns, *J. Fluid Mech.* **508**, 175 (2004).
 - [10] E. Lajeunesse, A. Mangeney-Castelnau, and J. Vilotte, Spreading of a granular mass on a horizontal plane, *Phys. Fluids* **16**, 2371 (2004).
 - [11] Y. Zhou, P.-Y. Lagrée, S. Popinet, P. Ruyer, and P. Aussillous, Experiments on, and discrete and continuum simulations of, the discharge of granular media from silos with a lateral orifice, *J. Fluid Mech.* **829**, 459 (2017).
 - [12] D. Khakhar, J. McCarthy, and J. M. Ottino, Radial segregation of granular mixtures in rotating cylinders, *Phys. Fluids* **9**, 3600 (1997).
 - [13] S. Ji, D. M. Hanes, and H. H. Shen, Comparisons of physical experiment and discrete element simulations of sheared granular materials in an annular shear cell, *Mechanics of materials* **41**, 764 (2009).
 - [14] E. Azanza, F. Chevoir, and P. Moucheron, Experimental study of collisional granular flows down an inclined plane, *J. Fluid Mech.* **400**, 199 (1999).
 - [15] S.-C. Yang and S.-S. Hsiau, The simulation and experimental study of granular materials discharged from a silo with the placement of inserts, *Powder Technology* **120**, 244 (2001).
 - [16] A. V. Orpe and D. Khakhar, Rheology of surface granular flows, *J. Fluid Mech.* **571**, 1 (2007).
 - [17] M. I. Arran, A. Mangeney, J. De Rosny, M. Farin, R. Toussaint, and O. Roche, Laboratory earthquakes: Insights from experiments into the high-frequency seismic signal generated by geophysical granular flows, *Journal of Geophysical Research: Earth Surface* **126**, e2021JF006172 (2021).
 - [18] V. Bachelet, A. Mangeney, R. Toussaint, J. de Rosny, M. I. Arran, M. Farin, and C. Hibert, Acoustic emissions of nearly steady and uniform granular flows: A proxy for flow dynamics and velocity fluctuations, *Journal of Geophysical Research: Earth Surface* **128**, e2022JF006990 (2023).
 - [19] L. E. Silbert, D. Ertas, G. S. Grest, T. C. Halsey, D. Levine, and S. J. Plimpton, Granular flow down an inclined plane: Bagnold scaling and rheology, *Phys. Rev. E* **64**, 051302 (2001).

- [20] F. Da Cruz, S. Emam, M. Prochnow, J.-N. Roux, and F. Chevoir, Rheophysics of dense granular materials: Discrete simulation of plane shear flows, *Phys. Rev. E* **72**, 021309 (2005).
- [21] O. Pouliquen, C. Cassar, P. Jop, Y. Forterre, and M. Nicolas, Flow of dense granular material: towards simple constitutive laws, *Journal of Statistical Mechanics: Theory and Experiment* **2006**, P07020 (2006).
- [22] O. Baran, D. Ertaş, T. C. Halsey, G. S. Grest, and J. B. Lechman, Velocity correlations in dense gravity-driven granular chute flow, *Phys. Rev. E* **74**, 051302 (2006).
- [23] T. Börzsönyi, R. E. Ecke, and J. N. McElwaine, Patterns in flowing sand: understanding the physics of granular flow, *Phys. Rev. Lett.* **103**, 178302 (2009).
- [24] A. Tripathi and D. Khakhar, Rheology of binary granular mixtures in the dense flow regime, *Phys. Fluids* **23**, 113302 (2011).
- [25] V. Kumaran and S. Bharathraj, The effect of base roughness on the development of a dense granular flow down an inclined plane, *Phys. Fluids* **25**, 070604 (2013).
- [26] N. Brodu, R. Delannay, A. Valance, and P. Richard, New patterns in high-speed granular flows, *J. Fluid Mech.* **769**, 218–228 (2015).
- [27] S. Mandal and D. V. Khakhar, A study of the rheology of planar granular flow of dumbbells using discrete element method simulations, *Phys. Fluids* **28**, 103301 (2016).
- [28] V. J.-L. Ralaïarisoa, A. Valance, N. Brodu, and R. Delannay, High speed confined granular flows down inclined: numerical simulations, in *EPJ Web of Conferences*, Vol. 140 (2017) p. 03081.
- [29] S. Mandal and D. Khakhar, A study of the rheology and micro-structure of dumbbells in shear geometries, *Phys. Fluids* **30**, 013303 (2018).
- [30] A. Bhateja and D. V. Khakhar, Rheology of dense granular flows in two dimensions: Comparison of fully two-dimensional flows to unidirectional shear flow, *Phys. Rev. Fluids* **3**, 062301 (2018).
- [31] A. Bhateja and D. V. Khakhar, Analysis of granular rheology in a quasi-two-dimensional slow flow by means of discrete element method based simulations, *Phys. Fluids* **32**, 013301 (2020).
- [32] S. Patro, M. Prasad, A. Tripathi, P. Kumar, and A. Tripathi, Rheology of two-dimensional granular chute flows at high inertial numbers, *Phys. Fluids* **33**, 113321 (2021).
- [33] B. Debnath, K. K. Rao, and V. Kumaran, Different shear regimes in the dense granular flow in a vertical channel, *J. Fluid Mech.* **945**, A25 (2022).
- [34] S. Patro, A. Tripathi, S. Kumar, and A. Majumdar, Unsteady granular chute flows at high inertial numbers, *Phys. Rev. Fluids* **8**, 124303 (2023).
- [35] Y. Forterre and O. Pouliquen, Flows of dense granular media, *Annu. Rev. Fluid Mech.* **40**, 1 (2008).
- [36] Y. F. B. Andreotti and O. Pouliquen, *Granular Media: Between Fluid and Solid* (Cambridge University Press, Cambridge, 2013).
- [37] P. Jop, Rheological properties of dense granular flows, *Comptes rendus physique* **16**, 62 (2015).
- [38] A. Tripathi, V. Kumar, A. Agarwal, A. Tripathi, S. Basu, A. Chakrabarty, and S. Nag, Quantitative dem simulation of pellet and sinter particles using rolling friction estimated from image analysis, *Powder Technology* **380**, 288 (2021).
- [39] Y. Lu, Z. Jiang, X. Zhang, J. Wang, and X. Zhang, Vertical section observation of the solid flow in a blast furnace with a cutting method, *Metals* **9**, 127 (2019).
- [40] T. Mitra, *Modeling of Burden Distribution in the Blast Furnace*, Ph.D. thesis (2016).
- [41] G. K. Barrios, R. M. de Carvalho, A. Kwade, and L. M. Tavares, Contact parameter estimation for dem simulation of iron ore pellet handling, *Powder Technology* **248**, 84 (2013), discrete Element Modelling.
- [42] H. Wei, H. Nie, Y. Li, H. Saxén, Z. He, and Y. Yu, Measurement and simulation validation of dem parameters of pellet, sinter and coke particles, *Powder Technology* **364**, 593 (2020).
- [43] Y. Yu and H. Saxén, Flow of pellet and coke particles in and from a fixed chute, *Industrial & Engineering Chemistry Research* **51**, 7383 (2012).
- [44] Y. Yu and H. Saxén, Particle flow and behavior at bell-less charging of the blast furnace, *steel research international* **84**, 1018 (2013).
- [45] J. Tang, X. Zhou, K. Liang, Y. Lai, G. Zhou, and J. Tan, Experimental study on the coefficient of restitution for the rotational sphere rockfall, *Environmental Earth Sciences* **80**, 419 (2021).
- [46] Y. Ye, Y. Zeng, K. Thoeni, and A. Giacomini, An experimental and theoretical study of the normal coefficient of restitution for marble spheres, *Rock Mechanics and Rock Engineering* **52**, 1705 (2019).